
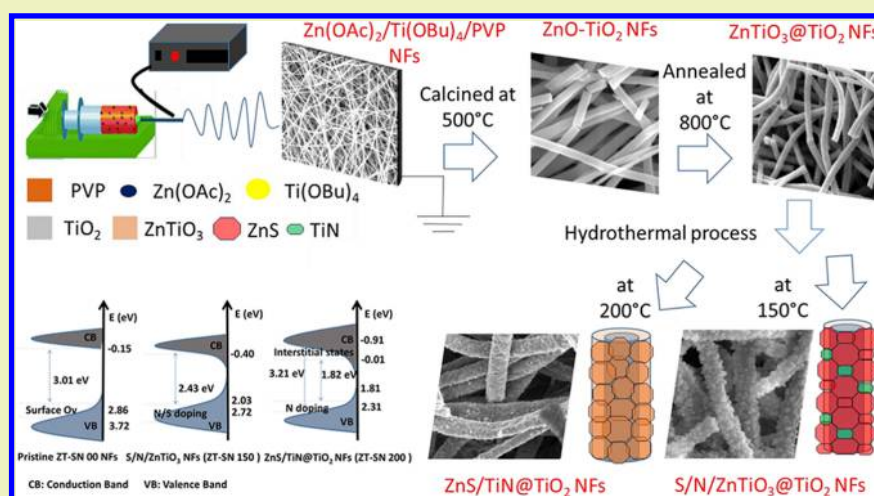


# Conscientious Design of Zn-S/Ti-N Layer by Transformation of ZnTiO<sub>3</sub> on Electrospun ZnTiO<sub>3</sub>@TiO<sub>2</sub> Nanofibers: Stability and Reusable Photocatalytic Performance under Visible Irradiation

Kugalur Shanmugam Ranjith\* and Tamer Uyar\*<sup>ID</sup>

Institute of Materials Science &amp; Nanotechnology and UNAM-National Nanotechnology Research Center, Bilkent University, Ankara 06800, Turkey

 Supporting Information

**ABSTRACT:** Herein, we report the rational design of Zn-S/Ti-N on TiO<sub>2</sub> as a hierarchical nanoarchitecture from the ZnTiO<sub>3</sub>@TiO<sub>2</sub> nanofibers (NFs) through electrospinning followed by a hydrothermal process using L-cysteine as an S/N source. Controlling the hydrothermal temperature, the hierarchical form of NFs exhibited highly efficient visible catalytic behavior for organic dye (i.e., Rhodamine B) degradation since S and N based surface function on the oxide surface resulted in unique interlayer induced strain coupled surface defects. The surface functionalization of the ZnTiO<sub>3</sub> surface with S and N was solidly confirmed by X-ray photo-electrospectroscopy (XPS) and energy-dispersive X-ray (EDX) with elemental mapping results. Inducing the S/N functionality at higher hydrothermal temperature reverses the structural arrangement of ZnTiO<sub>3</sub> favoring the interaction of S preferably with Zn and Ti with N for the formation of ZnS/TiN@TiO<sub>2</sub> NFs. The tunable band function through the Zn-S/Ti-N cofunctionalization exhibited effective long-term catalytic performance under UV and visible irradiation with a degradation rate of 0.0362 and 0.0313 min<sup>-1</sup>, which is nearly 3.1 and 1.3 times higher than that of the ZnTiO<sub>3</sub>@TiO<sub>2</sub> and ZnTiO<sub>3</sub>-S/N@TiO<sub>2</sub> NFs, respectively. The catalysts are highly photoactive after multiple photocatalytic cycles with stable surface and structural features under visible irradiation. The study could provide new opportunities for designing hierarchical structures in ternary form of nanoscale architectures for effective visible photocatalytic activity.

**KEYWORDS:** ZnTiO<sub>3</sub> nanofibers, Electrospinning, Hierarchical heterostructures, ZnS shell layers, S/N codoping, Visible photocatalysis, Solar irradiation

## INTRODUCTION

Over the concern of extreme textile and organic industrial wastewater pollution, environment remediation is taken up to enable the world to step forward with various technologies for the development of wastewater treatment.<sup>1,2</sup> Photoresponsive advanced oxidation processes through a heterostructural catalyst are intended toward the degradation or removal of organic pollutants from wastewater. In this context, TiO<sub>2</sub> and ZnO are the most promising semiconductor photocatalysts with their wide band gap function facilitating their exploration for wastewater treatment. However, both these semiconductors

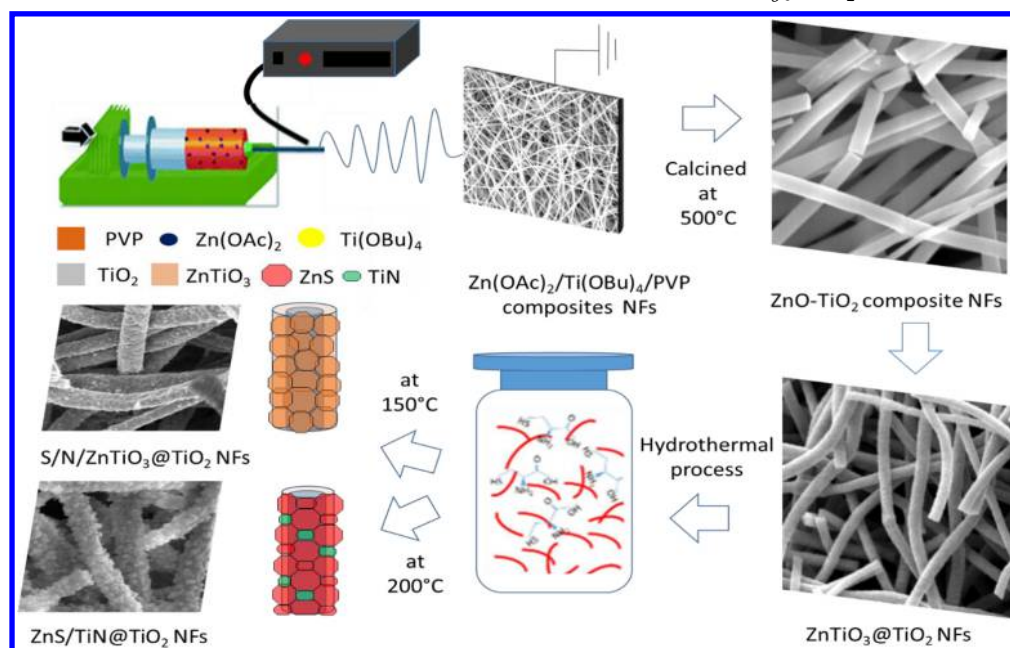
have their individual advantages and disadvantages when it comes to their catalytic efficiency under UV irradiation owing to the favorable wide band gap (>3.2 eV).<sup>3,4</sup> Alloying these wide band gap materials in the form of ternary oxides such as ZnTiO<sub>3</sub> favors a similar band function, overcoming their structural disadvantages.<sup>5,6</sup> It is a known fact that UV photon energy accounts only for nearly 5% of total solar energy, which

Received: May 28, 2018

Revised: July 26, 2018

Published: August 26, 2018



Scheme 1. Synthesis Process for the Hierarchical Formation of S/N Modified  $\text{ZnTiO}_3/\text{TiO}_2$  NFs

is very low when compared to 45% of visible photon energy.<sup>7</sup> In order to commercialize advanced oxidation process based wastewater treatments, solar energy has to be utilized, and semiconductor nanostructures have to be developed in such a way that they effectively drive visible catalytic behavior.<sup>8</sup> Doping and decoration of metallic or nonmetallic elements with wide band gap semiconductors improved visible catalytic behavior by narrowing the band gap or its band function.<sup>9–12</sup> In that, doping of nonmetallic elements such as N, C, S, and F plays an effective role as anionic impurities in the host lattice, thereby narrowing the band gap toward visible catalytic behavior.<sup>13</sup> Among the nonmetallic ions, S and N have garnered notable attention over the wide band gap materials with extended thermal stability and improvised visible response.<sup>14</sup> Doping with the cofunctionality of S and N has become attractive because of its tunable electronic structure which permits visible absorption in wide band gap semiconductors.<sup>15</sup> The favorable morphology with the 1D structural feature directs electron flow with high surface area and promotes the light responsive nature. Without disturbing the morphological features, inducing the S/N codopants in the single set synthesis process is highly complicated and only leads to a low content of S impurities on the catalyst surface. Postsynthesis of S/N codoping functionality through a hydrothermal process shows promise in nonmetal doped catalyst platforms, which can be created through the diffusion of S and N ions. Further processing the postsynthesis process to modify the surface features of the nanostructures to S and N based compounds with a heterostructural finish helps in improving the visible response and promotes charge separation efficiency. In the case of codoping functionality, L-cysteine is one of the effective sources of S and N ions to obtain improvised structural features on the catalytic surface. Previously, there were few investigations which found that, L-cysteine plays a role in the construction of S/N cofunctionalized surfaces for tunable functional properties.<sup>16,17</sup> Controlled release and interaction of  $\text{S}^{2-}$  and N ions through the hydrothermal process favors the surface functionality with tunable band function over the semiconductor surface.<sup>18</sup> From

the observations attained from our previous investigations, Zn ions were more favorable for the sulfidation reaction, and Ti ions interact poorly with S ions, thereby leading to promising interactions with Zn sites.<sup>19,20</sup> Further, there is an interesting possibility of an interaction of Ti–N sites on the surface by a nitration process at higher temperatures, which will lead to the hierarchical heterostructural finish.<sup>21,22</sup> Combining the sulfidation and nitration process on the  $\text{ZnTiO}_3$  surface would create a new structural feature with the role of S and N based interstitial structures with tunable band functionalities of Zn–S and Ti–N interactions. The exploration of the dual functionality of S and N ions over the  $\text{ZnTiO}_3$  nanostructures facilitates extended visible catalytic behavior.

This work signifies the synthesis of the dual functionalization of S and N cocatalyzed  $\text{ZnTiO}_3/\text{TiO}_2$  nanofibers (NFs) through electrospinning followed by a hydrothermal process as shown in Scheme 1. The temperature influences the hydrothermal process to modify the S and N impurities to form as a ZnS–TiN surface functionality on  $\text{TiO}_2$  NFs through the selective interaction with Zn ions by sulfidation and Ti by the nitration process. Electrospun NFs of titanium butoxide, zinc acetate, and PVP composites were calcined to form  $\text{TiO}_2$ – $\text{ZnTiO}_3$  NFs depending on the ionic concentration of Zn ions on the fiber surface under high annealing temperature. Also, the process of hydrothermal treatment with L-cysteine serves as the S and N source for obtaining dual functionality. The temperature of the hydrothermal process plays a crucial role in the S ionic state and structural morphology of the fibers with the Zn–S/Ti–N layer by transforming  $\text{ZnTiO}_3$  over  $\text{TiO}_2$ . After adhering to the presence of the S/N functionality over the  $\text{ZnTiO}_3/\text{TiO}_2$  NFs through the EDAX and XPS studies, visible catalytic activity and long-term catalytic stability were investigated. After repeated photocatalytic cycles, the stable structural form of the S/N– $\text{ZnTiO}_3$  surface finish exhibited efficient catalytic activity under visible irradiation.

## EXPERIMENTAL SECTION

**Materials.** Polyvinylpyrrolidone (PVP,  $M_w = 1,300,000$ , Sigma-Aldrich, CAS No.: 9003-39-8), zinc acetate ( $\text{Zn}(\text{OAc})_2$ , Sigma-

Aldrich, CAS No.: 5970-45-6), titanium(IV) butoxide ( $\text{Ti}(\text{OBU})_4$ , Sigma-Aldrich, CAS No.: 5593-70-4), ethanol ( $\text{C}_2\text{H}_5\text{OH}$ , Sigma-Aldrich, CAS No.: 64-17-5), L-cysteine (97%,  $\text{HSCH}_2\text{CH}(\text{NH}_2)\text{CO}_2\text{H}$ , Sigma-Aldrich, CAS No.: 52-90-4), acetic acid ( $\text{CH}_3\text{COOH}$ , Sigma-Aldrich, CAS No.: 64-19-7), rhodamine B (RhB, Sigma-Aldrich, CAS No.: 81-88-9), methylene blue (MB, Sigma-Aldrich, CAS No.: 122965-43-9), 4-chlorophenol (99%, 4-CP, Alfa Aesar, CAS No.: 106-48-9), *p*-benzoquinone (98%, BQ, Alfa Aesar, CAS No.: 106-51-4), triethanolamine, (99%, TEOA, Sigma-Aldrich, CAS No.: 102-71-6), and isopropyl alcohol (99.5% IPA, Sigma-Aldrich, CAS No.: 67-63-0) were procured and were used as received without any further purification.

**Electrospinning of  $\text{ZnTiO}_3/\text{TiO}_2$  NFs.**  $\text{TiO}_2$ – $\text{ZnTiO}_3$  NFs were synthesized using an electrospinning process followed by the high temperature calcination process. PVP (1 g) was dissolved in 5 mL of ethanol by constant stirring as an electrospinning solution. As the Ti and Zn precursors, 1 mL of  $\text{Ti}(\text{OBU})_4$  and 4% (w/v) of  $\text{Zn}(\text{OAc})_2$  were mixed in 2 mL of ethanol and 0.6 mL of acetic acid solution and stirred. After attaining a homogeneous clear solution, it was added into the polymeric solution and stirred overnight before the electrospinning process. The attained homogeneous solution was loaded in a 3 mL plastic syringe with a needle diameter of 0.4 mm and placed horizontally on a syringe pump (KD Scientific, KDS101). Under the applied high electric field (15.0 kV) from a high voltage power supply (Spellman, SL series, USA) with a solution flow rate of  $0.5 \text{ mL h}^{-1}$ , the electrospun NFs were collected on the aluminum foil cover metal collector placed at a distance of 15 cm from the needle tip. This whole process was carried out at  $22^\circ\text{C}$  and 19% relative humidity in a Plexiglas box. The obtained electrospun  $\text{Zn}(\text{OAc})_2/\text{Ti}(\text{OBU})_4/\text{PVP}$  composite NFs were further calcined at  $500^\circ\text{C}$  for 3 h in air to remove the organic moiety to form  $\text{ZnO-TiO}_2$  composite NFs, followed by annealing at  $800^\circ\text{C}$  for 3 h, which favors the formation of  $\text{TiO}_2$ – $\text{ZnTiO}_3$  (ZT-SN 00) NFs. Annealing at high temperature causes Zn ions to move toward the surface and be substituted with Ti ions to form the  $\text{ZnTiO}_3$  surface finish with a wall thickness of 100 nm. The wall thickness depends on the ionic concentration of the Zn in the composite fibers, and herein, we use 4 wt % of Zn precursor concentration.

**Synthesis of S/N-Doped- $\text{ZnTiO}_3/\text{TiO}_2$  and  $\text{ZnS}/\text{TiN}/\text{TiO}_2$  NFs.** To synthesize the hierarchical functionality of the S/N modified  $\text{ZnTiO}_3$  surface, pristine ZT-SN 00 NFs (0.05 g) and L-cysteine (0.02 g) were added to 40 mL of deionized water under stirring. After continuous stirring for 30 min at room temperature, the solution was transferred to a 50 mL Teflon autoclave and held at different temperatures (100, 150, and  $200^\circ\text{C}$ ) for 6 h. As per the hydrothermal temperature, the samples were named as ZT-SN 00, ZT-SN 100, ZT-SN 150, and ZT-SN 200 for the pristine, 100, 150, and  $200^\circ\text{C}$  of hydrothermally grown samples. After the sample cooled down, precipitates were centrifuged and washed with water and ethanol thrice and dried at  $80^\circ\text{C}$  for 60 min. Dried samples were calcined at  $200^\circ\text{C}$  for 2 h in vacuum, which resulted in the ZT-SN NFs with different S and N functionalities.

**Characterization.** Scanning electron microscopy (SEM, FEI-Quanta 200 FEG) equipped with an energy dispersive X-ray spectrometer (EDS) was used to characterize the morphological and elemental composition of the electrospun nanostructures. The structural features of the ZT-SN samples were measured by a PANalytical X'Pert multipurpose X-ray diffractometer with  $\text{Cu K}\alpha$  radiation. Transmission electron microscopy (FEI-Tecnaï G2 F30) with an accelerating voltage of 200 kV was used to investigate morphological features of the NFs. Elemental mapping was carried out using scanning transmission electron microscopy (STEM, Tecnaï G2 F30, FEI). UV–vis diffuse reflectance spectra were obtained on an UV–vis spectrophotometer (Shimadzu UV-3600 spectrophotometer), and the band gap of the surface modified nanostructures were calculated through the transformed Kubelka–Munk relationship. X-ray photoelectron spectroscopy (XPS, Thermo K-alpha-monochromated) was employed to analyze the surface chemical composition. Photoluminescence (PL) measurements were performed by using a time-resolved fluorescence spectrophotometer (FL-1057 TCSPC)

with an excitation wavelength at 350 nm. The specific surface area of the samples were analyzed using the Brunauer–Emmet–Teller (BET) method carried out on a Quantachrome Instrument autosorb ( $iQ_2$ ) analyzer after degassing the samples for 3 h at  $200^\circ\text{C}$ . Dye degradation was analyzed by the UV–vis absorbance spectra of pollutants using an UV–vis spectrophotometer (Varian Cary 100).

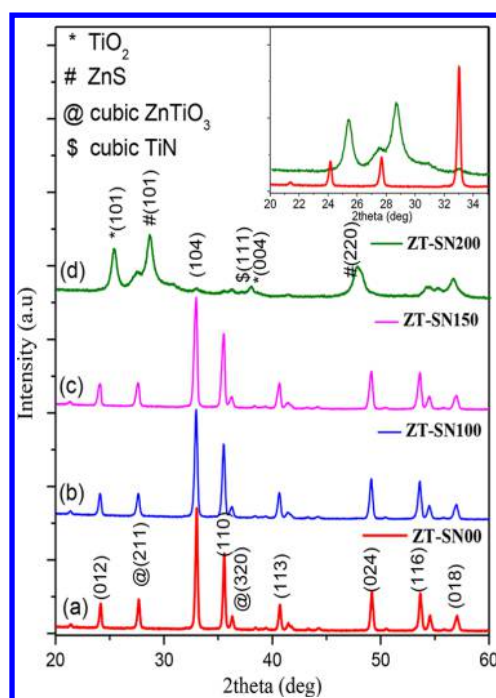
**Photocatalytic Degradation.** Catalytic degradation was done under UV irradiation (Ultra-Vitalux Ultraviolet high pressure lamp (300 W, Osram)  $\lambda \sim 365 \text{ nm}$ , 272 lx of photon energy), visible irradiation (75 W, Osram), xenon lamp with UV filter ( $\lambda > 400 \text{ nm}$ , 560 lx of photon energy), and natural sunlight ( $\lambda > 400 \text{ nm}$ ,  $860 \times 100 \text{ lx}$  of photon energy) (with UV cutoff filter (Lee type 226 (USA)) at room temperature using RhB as the probe molecule. In separate quartz cuvettes, 1 mg/mL of electrospun ZT-SN based NFs were immersed with RhB dye solution (10 ppm) and placed in the dark for 20 min to attain the adsorption/desorption equilibrium of dye on the NF surface before photoirradiation. The working distance between the lamp and the sample was set to be 15 cm, and a series of samples and controls (without catalyst) were simultaneously irradiated. The degradation of RhB dye molecules was monitored from the real time absorption intensity at 554 nm, and the relative concentrations of the pollutants ( $C/C_0$ ) evaluated the photocatalytic activities with respect to time using a UV–vis spectrophotometer. The catalytic behavior was investigated in sunlight ( $>400 \text{ nm}$ ) under the shadow from 9:00 am to 3:00 pm during a sunny day. The average light intensity of sunlight was  $860 \times 100 \text{ lx}$ . In order to investigate the long-term stability, the reusability of the catalysts over 10 consecutive cycles was tested under visible irradiation. The degradation efficiency of dye solution was calculated by  $((C_0 - C)/C_0) \times 100$ , where  $C$  and  $C_0$  denote the UV-absorption peak intensity before and after UV and visible irradiation. Further, photocatalytic degradation activity over another dye molecule (MB (15 ppm)) and colorless organic waste (4-CP (10 ppm)) were investigated.

**Active Species Trapping Experiments.** To quantify the production of active radicals such as hydroxyl radicals ( $^\circ\text{OH}$ ), superoxide radicals ( $\text{O}_2^\circ$ ), and holes ( $\text{h}^+$ ) on the photocatalytic reaction, 1.0 mM BQ (a quencher of  $\text{O}_2^\circ$ ), IPA (a quencher of  $^\circ\text{OH}$ ), and TEOA (a quencher of  $\text{h}^+$ ) were added to the photocatalytic reaction with the catalyst.<sup>19</sup> The method was similar to a former photocatalytic activity test.

## RESULTS AND DISCUSSION

**Structural and Morphological Studies.** Scheme 1 represents the systematic procedure for preparing Zn-S/Ti-N and S/N- $\text{ZnTiO}_3$  layers from the pristine  $\text{ZnTiO}_3$  layer on  $\text{TiO}_2$  NFs through the feasible construction of electrospinning followed by a hydrothermal process. The bead-free fibrous network having an average fiber diameter of  $625 \pm 45 \text{ nm}$  with the composition of  $\text{Zn}(\text{OAc})_2/\text{Ti}(\text{OBU})_4/\text{PVP}$  was revealed from the SEM images in Figure S1. After calcination at  $500^\circ\text{C}$  for 3 h, it exhibited the formation of  $\text{ZnO-TiO}_2$  composite NFs with a fiber diameter of  $425 \pm 85 \text{ nm}$  (Figure S2) by completely removing the organic part (PVP polymer matrix and acetate and butoxide group). Furthermore, on annealing the composite NFs at  $800^\circ\text{C}$ , the formation of  $\text{ZnTiO}_3$  NFs was favored. The obtained NFs were subjected to functionalization of S/N through a hydrothermal process, favoring the formation of S/N doped  $\text{ZnTiO}_3$  NFs. In Figure 1, crystalline phases of S/N modified  $\text{ZnTiO}_3$  NFs were investigated through an X-ray powder diffraction (XRD) pattern. Figure 1a exhibited the crystalline nature of the pristine  $\text{ZnTiO}_3$  NFs annealed at  $800^\circ\text{C}$ . On annealing the electrospun NFs at  $800^\circ\text{C}$ , they change to the crystal phase of the hexagonal  $\text{ZnTiO}_3$ , which matches with the JCPDS card no. of 26-1500 with a cubic phase. No additional peaks representing  $\text{TiO}_2$  or  $\text{ZnO}$  in the pattern was found, which confirmed the purity of the  $\text{ZnTiO}_3$  nanostructure (Figure 1a). After annealing at  $800^\circ\text{C}$ ,

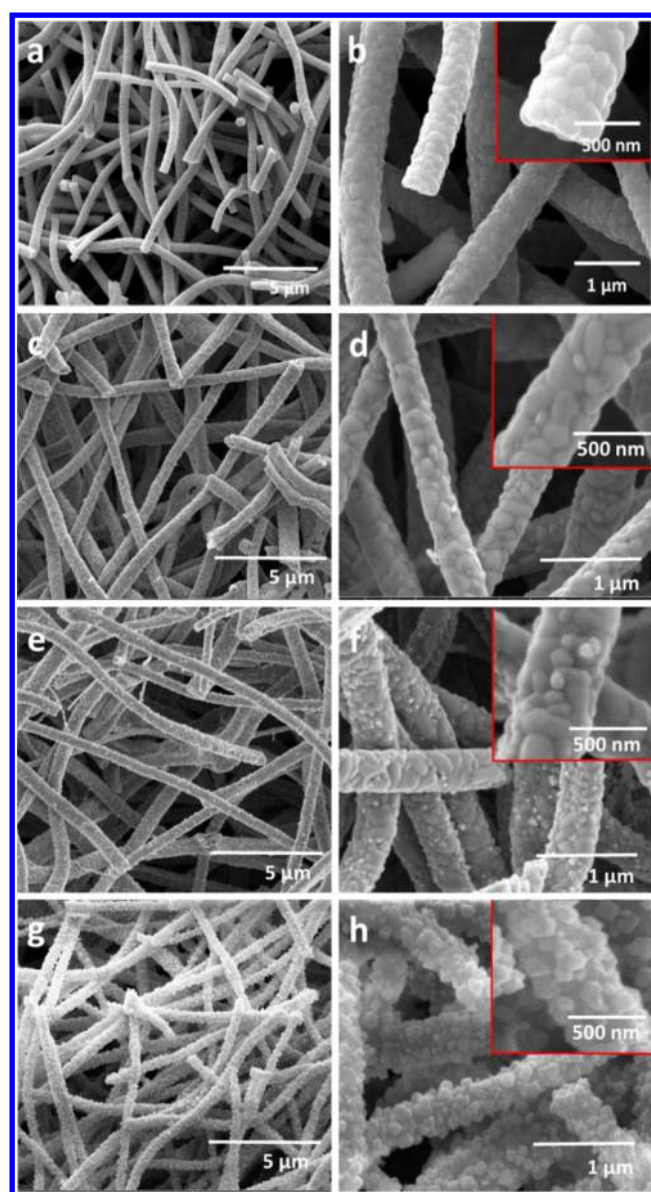




**Figure 1.** XRD patterns of the ZT-SN based NFs (a) ZT-SN 00 NFs, (b) ZT-SN 100, (c) ZT-SN 150, and (d) ZT-SN 200.

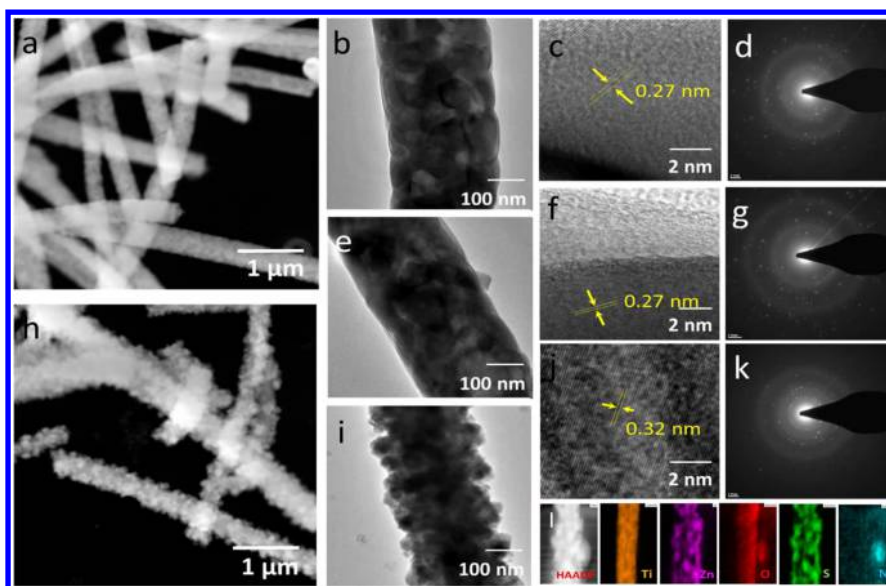
ZnTiO<sub>3</sub> NFs were formed, while annealing below 800 °C exhibited a mixed phase consisting of ZnTiO<sub>3</sub>, ZnO, and TiO<sub>2</sub>. However, the actual assembly of the NFs consists of the ZnTiO<sub>3</sub>@TiO<sub>2</sub> based structural finish, which was later confirmed by the TEM image mapping analysis. Because of the highly crystalline solid 100 nm wall thickness of the ZnTiO<sub>3</sub> layer, peaks corresponding to TiO<sub>2</sub> were absent in the pattern but were present as a central core on the annealed NF finish (Figure S3). On treating ZnTiO<sub>3</sub> NF with L-cysteine by the hydrothermal process, no other additional diffraction peaks were observed until 150 °C (Figure 1b,c), but while treating ZnTiO<sub>3</sub> with L-cysteine by hydrothermal process at 200 °C, a change in diffraction pattern representing the crystal planes of anatase phase of TiO<sub>2</sub> (JCPDS card no. 21-1272) and the hexagonal phases of ZnS (JCPDS card no. 36-1450) with the suppressed diffraction peaks of ZnTiO<sub>3</sub> was exhibited. Additionally, a mild trace of new peaks at 37.1 and 43.2 was identified, which corresponds to the (111) and (200), respectively, of the crystal structure of the cubic TiN (JCPDS-38-1420). This observation suggest that the wall of ZnTiO<sub>3</sub> was transformed to ZnS and TiN after the 200 °C hydrothermal treatment of L-cysteine. To observe the clear origin of the spectral intensity of the ZnS and TiN crystal lattice, the pattern is presented in the log scale (Figure S4).

The SEM (Figure 2) and TEM (Figure 3) investigations reveal the structural features of NF morphology and exhibit the surface features respective to the thermal treatment and sulfur functionalization. As shown in Figure S2, after calcination at 500 °C to remove the organic content, the NFs exhibited grains with the average diameter of 425 ± 85 nm. Further annealing of the NFs at 800 °C (diameter of 400 ± 50 nm) reveals the formation of densely packed grains with the size of 90 ± 10 nm, as shown in Figure 2a,b; the surface grains appeared to be bound to each other and exhibited a solid fiber network. On hydrothermally treating the ZnTiO<sub>3</sub> NF with L-cysteine at 100 °C, the surface of the NFs had a morphology



**Figure 2.** SEM and magnified SEM images of the S modified ZT-SN NFs. (a,b) Pristine ZT-SN 00 NFs, (c,d) ZT-SN 100, (e,f) ZT-SN 150, and (g,h) ZT-SN 200.

similar to that of ZT-SN 00 NFs (Figure 2c,d), but on treating the fibers under 150 °C, the surface of ZnTiO<sub>3</sub> NFs was quite modified with nanograins decorated around with a size of 20–30 nm. On further increasing the hydrothermal temperature, ZnTiO<sub>3</sub> NFs clearly exhibited a change in morphology after the S/N modification at 200 °C (Figure 2g,h). A notable change in surface features after the hydrothermal process implies S/N modification over the ZnTiO<sub>3</sub> NFs. The S/N modification favors the considerable increase in surface features with smaller grains, without disturbing the morphology of the NFs. Figure 2h clarifies the smaller grain assembly after the hydrothermal process with the average size ca. 40 nm of surficial grains. EDAX spectra reveals the prominent exhibition of S ions after 200 °C of hydrothermal treatment on the ZnTiO<sub>3</sub> layer (Figure S5) as compared with the pristine ZT-SN 00 NFs and low temperature hydrothermally treated samples. Formation of S/N modified ZnTiO<sub>3</sub> NFs can be explained by the diffusion migrations of S ions over the metal



**Figure 3.** STEM, TEM, and HRTEM images of the as-prepared ZT-SN 00 NF (a,b,c,d), ZT-SN 150 NF (e,f), and ZT-SN 200 NF (h,i,j). (d,g,k) SAED pattern image of pristine ZT-SN 00, ZT-SN 150, and ZT-SN 200 NF. (l) EDAX mapping results of ZT-SN 200 NF.

oxide surface through the Kirkendall effect under thermally activated conditions. It clearly exhibits that after the decomposition temperature of L-cysteine (160 °C), functionally broken S and N ions favored the surface interaction with the ZnTiO<sub>3</sub> NF surface and modified its crystal structure.<sup>23,24</sup>

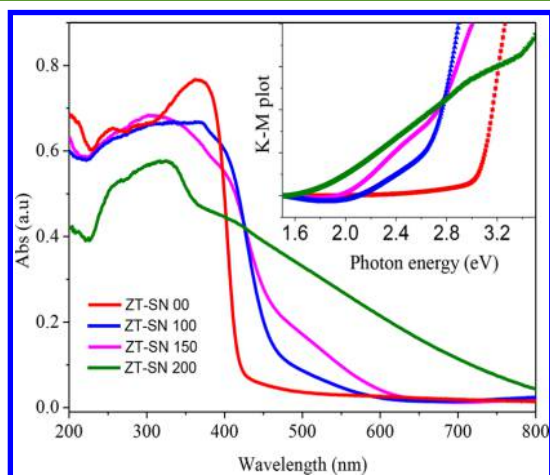
TEM images of pristine ZT-SN 00 NF reveal (Figure 3a,b) the solid core feature of the fiber morphology with a closely packed grain assembly. Each grain has an average size around 80–100 nm. The elemental mapping results evidence the intended core of Ti–O ionic distribution as compared with the surface level, which evidenced the formation of the ZnTiO<sub>3</sub>@TiO<sub>2</sub> NF feature. This may be due to the annealing effect, which induces the mobility of Zn ions to the surface forming ZnTiO<sub>3</sub> with the TiO<sub>2</sub>. Because of the solid grain assembly with higher crystalline quality, this feature was not detected through XRD analysis. Under the hydrothermal treatment at 150 °C with L-cysteine, there was no notable surface modification apart from the exhibition of small surface grains (Figure 3e). HRTEM images (Figure 3f) revealed that the exhibition of unchanged lattice spacing of 0.27 nm represented the ZnTiO<sub>3</sub> lattice along the (104) planes.<sup>6</sup> On functionalizing the ZnTiO<sub>3</sub>@TiO<sub>2</sub> NF with L-cysteine under the hydrothermal process at 200 °C, the surface interacted with the S and N ions and exhibited surface modified nanograined (20–40 nm) functionalization (Figure 3h, i). The HRTEM images of the pristine and L-cysteine treated ZnTiO<sub>3</sub>@TiO<sub>2</sub> NF clearly revealed a change in surface grain lattice space variation from 0.27 to 0.32 nm, which indicates that the surface of ZnTiO<sub>3</sub> was modified at higher temperature hydrothermal processes. The change in the lattice spacing difference after the hydrothermal process revealed that the outer surface was transformed to ZnS nanograins with the lattice spacing of 0.32 nm. The marked interplanar *d* spacing signifies the (011) zone axis which represents the hexagonal ZnS.<sup>25</sup> After the deformation of the ZnS from ZnTiO<sub>3</sub>, the surface grains were pragmatically exhibited in the form of loosely bonded individual nanograins at the surface without any secondary particle arrangement.<sup>26</sup> Figure 3d, g, and k represents the SAED pattern of the as-prepared ZT-SN 00 NFs, ZT-SN 150 NFs, and ZT-SN 200 NFs, respectively. The SAED pattern

indicates the polycrystalline nature of the fiber surface with change in *d*-spacing with respect to the interaction of S ions on the surface. At high temperature, the surface was completely modified as the ZnS nanograin assembly with a solid TiO<sub>2</sub> core, which is clearly evidenced from the EDAX elemental mapping analysis over the 200 °C hydrothermally treated NFs. The 150 °C hydrothermally treated NFs show that S and N were functionalized on the NF surface without disturbing the morphology, which is shown in Figure 3l, Figure S6, and Figure S7.

The EDAX mapping profile reveals that when L-cysteine interacts with the ZnTiO<sub>3</sub> surface, S ions interact with the Zn sites and convert it as Zn–S, which forms the ZnS on TiO<sub>2</sub> NF, and additionally, there is a possibility of N interaction of the fiber surface which evidence the presence of the Ti–N interface on the fiber morphology. The additional interesting feature observed from XRD and EDAX mapping is that in the hydrothermal process, at 200 °C there was a promising exhibition of TiO<sub>2</sub> and ZnS/TiN crystal grains with hierarchical assembly but that the surface was not covered uniformly because of the deformation of ZnTiO<sub>3</sub> into ZnS and TiN. The deformation of ZnTiO<sub>3</sub> into Zn–S and Ti–N leads to the possibility of leaching of unreacted metal ions, which causes the uncovered surface layer on TiO<sub>2</sub> NF. In the hydrothermal process (200 °C), S ions interact with the Zn ions, which later form as ZnS, and the N ions reacted with the Ti ions to form Ti–N on the surface. The presence of Ti ions on the ZnTiO<sub>3</sub> NF surface was nearly left unreactive with S ions and were dissolved in the precursor solution or leached from the surface during the hydrothermal process. This conventional process reveals the exhibition of ZnS, TiN, and TiO<sub>2</sub> phases in XRD, and in the image mapping, TiO<sub>2</sub> forms the core with the ZnS functionality with a mild trace of N throughout the NF surface. After surface modification through the hydrothermal process, the specific surface area of the ZT-SN samples increased due to the high surface features as 16.0 m<sup>2</sup>/g and 40.3 m<sup>2</sup>/g, for the pristine ZT-SN 00 and ZT-SN 200, respectively. From the comparative results, ZT-SN 200 shows the higher specific surface area, which is more than twice higher than the pristine NFs (Figure S8).



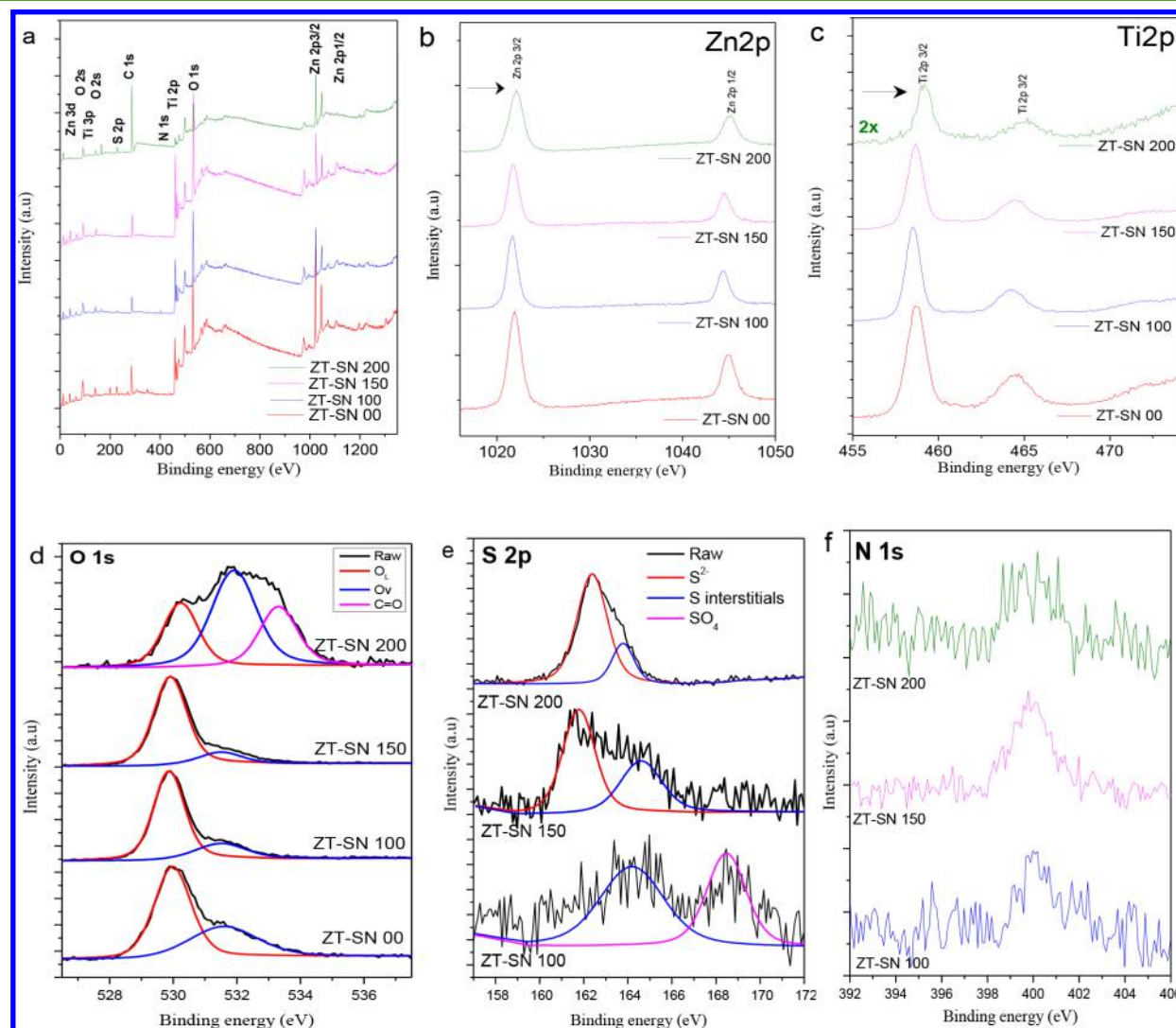
**Optical Studies.** Figure 4 shows the UV–vis diffuse reflectance absorption spectra of the S/N-ZnTiO<sub>3</sub> NF as a



**Figure 4.** UV–vis diffuse reflectance spectra of the pristine and S/N functionalized ZT-SN NFs. The inset shows the K-M function of the respective spectra.

function of hydrothermal temperature. On comparing with the pristine, ZT-SN NFs exhibited a blue shift at maximum absorption, but the absorption edge red-shifted toward the visible region. The inset shows the K-M plot of the ZT-SN NF with respect to the hydrothermal temperature. The pristine ZT-SN 00 NF reveals a sharp slope at the absorption edge in the UV region corresponding to the band edge absorption with a band gap of 3.01 eV. At lower hydrothermal temperature, the band gap slightly reduced (2.6 eV) due to the nitrogen and sulfur doping functionality above the valence band (VB), but interestingly, ZT-SN 200 samples show dual band edge absorption around 3.00 eV and shallow level of extended band edge absorption toward the visible region up to 1.8 eV.

The possibility of the band edge at the UV region may be due to the TiO<sub>2</sub> NF and ZnS (and the extended visible absorption may be due to the interaction of Zn-S and Ti-N based surface functionality on the wide band gap TiO<sub>2</sub> NF or through the doping of N ion on the surface). The extended possibility of visible absorption may be due to the N subband levels on the ZnS and TiO<sub>2</sub> surface, created during the hydrothermal process. As observed from the previous investigations, the effective role of ZnS as a layer on a wide



**Figure 5.** XPS spectra of ZT-SN NFs. (a) Survey, (b) Ti 2p, (c) Zn 1s, (d) O 1s, (e) S 2p, and (f) N 1s signals taken from ZT-SN NFs synthesized at different hydrothermal temperatures.

band gap semiconductor would minimize the band function through the influence of band bending effect.<sup>19</sup> The effect of S functionality on the ZnTiO<sub>3</sub> NF extends the broadened absorption onset to 1.9 eV, which could be functionalized in the form of a type-II interface. The photographic images of the pristine and S/N modified ZT-SN NFs show the distinct color change from white to light orange after the hydrothermal process (Figure S9). The extended tail over the visible region represents band gap narrowing, which was attributed to the functionalization of the S and N atoms in the lattice of ZnTiO<sub>3</sub>. These functional atoms were occupied as the subband level between the valence band (VB) and conduction band (CB) states and reduced the electron transition energy and favored the narrow band function.

The surface chemical composition was explored by the XPS spectra (Figure 5) for the S/N functionalized TiO<sub>2</sub>–ZnTiO<sub>3</sub> NF. The survey spectra reveal (Figure 5a) a clear exhibition of O 1s, Ti 2p, Zn 2p, S 2p, N 1s, and C 1s core levels of the S/N modified ZnTiO<sub>3</sub> surface. The presence of the C 1s peak at 284.8 eV is attributed to the adventitious hydrocarbons generated by the XPS instrument and has been used as an internal reference. The high resolution Zn 2p XPS spectra (Figure 5b) shows the sharp characteristic edges at 1021.4 and 1044.5 eV, which represent the Zn 2p<sub>3/2</sub> and Zn 2p<sub>1/2</sub>, respectively.<sup>19</sup> The pronounced ratio of Zn/Ti (1.2) with the dominant exhibition of Zn at the surface has appeared in pristine ZT-SN NF. Functionalization with the S/N at different hydrothermal temperatures increases the Zn/Ti ratio. The absorbed mild shift from 1021.4 to 1022.1 eV may be due to the possibility of Ti–O–Zn–S or through the N–Zn–S based surface moieties. The split difference of 23.1 eV between the Zn 2p<sub>3/2</sub> and Zn 2p<sub>1/2</sub> core level components reveal the Zn<sup>2+</sup> state nature.<sup>19</sup> At higher hydrothermal temperature, the binding energy shifts with a notable difference which is reported to be the closest position of bulk ZnS, thereby signifying the Zn–S bond formation.<sup>25</sup> The high resolution scan of Ti 2p shows (Figure 5c) that for the pristine NFs two peaks were absorbed at 458.7 and 464.5 eV, which represent Ti 2p<sub>3/2</sub> and Ti 2p<sub>1/2</sub>, respectively. Sulfidation induced the shift in the binding energy from 458.7 to 459.2 eV, which is closer to the known TiO<sub>2</sub> (459.8 eV).<sup>20</sup> The strong interaction of Zn–S which results in the structural variation from Ti–O–Zn to ZnS leads to the binding energy shift, but the spectral space separation evidenced the existence of the Ti<sup>4+</sup> and Zn<sup>2+</sup> oxidation states. It further leads to the evidence that there is an observation of trivalent Ti<sup>3+</sup> formation during the hydrothermal process, which results from the Ti 2p<sub>3/2</sub> spectra. The intensity of the Ti was reduced for the ZT-SN 200 due to the removal or leaching of Ti at the surface, and the presence of Ti spectra may be due to the mild trace presence of Ti–N interaction and due to the exposure of the core surface by the uncovered surface layer. The oxygen vacancies (O<sub>v</sub>) induced to uphold the electrostatic balance which was confirmed by the existence of Ti<sup>3+</sup> with the substitution ratio of Ti<sup>4+</sup>/Ti<sup>3+</sup> in the ZnTiO<sub>3</sub> structure.<sup>27</sup> The semiquantitative analysis of the as-synthesized ZT-SN NFs is summarized in Table S1.

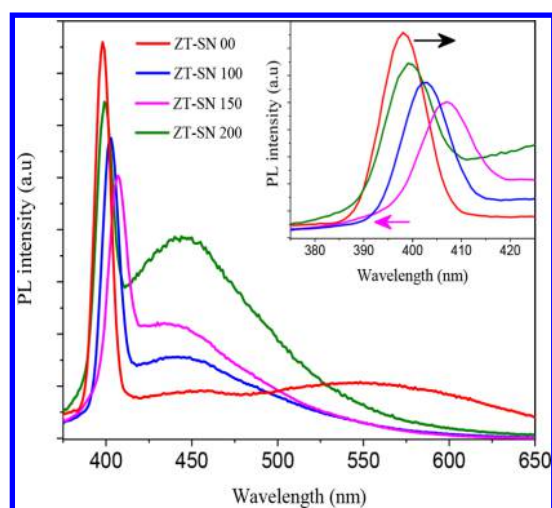
Figure 5d shows the higher resolution scanning of O 1s spectra of S/N functionalized samples fitted with the Gaussian function. The three split fitted peaks through the Gaussian function are represented as lattice oxygen (O<sub>L</sub>), O<sub>v</sub>, and chemisorbed oxygen ions (O<sub>C</sub>), respectively.<sup>19,20</sup> From the spectral observation, it clearly reveals that the intensity of O<sub>v</sub>

centered at 531 ± 0.4 eV was influenced by the sulfidation process. The drastic change in the ratio of O<sub>v</sub> on the ZT-SN 200 sample may be due to the formation of Zn–S nanograins with the existence of Ti<sup>3+</sup> functionality and the relative percentages of O<sub>L</sub> and O<sub>v</sub> with the function of sulfidation temperature as tabulated in Table S1. The reduction rate of O<sub>L</sub> on the ZT-SN 200 with other oxygen related peaks represents a promising interaction of the S ion with the ZnTiO<sub>3</sub> surface layer. The intensive modification of O<sub>v</sub> and O<sub>C</sub> on ZT-SN 200 samples reveals a promising surface modification through the sulfur interaction at higher temperature. The extended peak at 533.8 eV represents the interaction of C–O bonding on the fiber surface perhaps due to the decomposition of L-cysteine favoring the C interaction on the catalyst surface.

High resolution scanning of S 2p spectra of the S/N functionalized samples at different hydrothermal temperature is represented in Figure 5e. With the Gaussian function, the high resolution S 2p signal is split into three sets of peaks with different intensities at 162.2 eV, 164.2 eV, and 168.8 eV, which in turn represent the S lattice interaction, S interstitials, and SO<sub>4</sub> at the catalytic surface. Moreover, at lower hydrothermal (100 °C) temperature, S ions were just tagged with the ZnTiO<sub>3</sub> layer as SO<sub>4</sub> and S interstitial functionalities. On increasing the hydrothermal temperature, the relative intensities of these peaks completely change with strong interaction of S 2p on the NF surface with the possibility of a trace amount of S interstitials, possibly due to S doping on the ZnTiO<sub>3</sub> layer. At higher temperature (200 °C), the intense deconvoluted S 2p peak at 162.2 and 164.2 eV could represent S<sup>2–</sup> and S interstitials by the deformed chemical functionality of Ti–S and Zn–S.<sup>28,29</sup> At lower temperatures, the trace exhibition of SO<sub>4</sub> functionality (168.4 eV) reveals the interaction of oxygen sites of catalyst with the S ions. With increasing hydrothermal temperature, the lattice sulfur interaction with the metal ions increases in addition to the formation of S interstitials. In nature, the presence of S<sup>6+</sup> and S<sup>4+</sup> work as a surface trap for the photogenerated carriers which minimize the carrier recombination.<sup>20,30</sup> Further, the exhibition of S modification on the ZnTiO<sub>3</sub> NF surface induces the change in band function for the promotion of visible absorption behavior. The exhibited broad peak at 400 eV could represent the presence of N ions or N-doping in the NF surface (Figure 5f).<sup>31,32</sup>

The high resolution N 1s XPS spectra reveal the surface interaction of N species on the nanofibers by exhibiting the peaks at 396.4 and 399.6 eV. The previous investigations reveal that the interaction of N 1s around 396 eV evidence the substitution of nitrogen at the oxygen lattice such as Ti–N/Zn–N.<sup>33,34</sup> The peaks located around 400 eV represents different interstitial nitrogen species with strong oxygen adsorption on the fiber surface with the function of hydrothermal temperature.<sup>35</sup> The hydrothermal process induces the doping functionality of N ions on the fiber surface through the decomposition of L-cysteine where the N ions substitute the site of the oxygen and sulfur anions in the ZnTiO<sub>3</sub>, ZnS, and TiO<sub>2</sub> lattice, the metal nitride functionality, and N doped ZnS functionalities on the NF surface.<sup>31</sup> The relative atomic concentration of N ion in hydrothermally treated samples has been found to be 1.6, 2.4, and 3.6 at % for ZT-SN 100, ZT-SN 150, and ZT-SN 200 NF samples, respectively, based on the XPS data.

Figure 6 shows the photoluminescence spectra of the ZT-SN NF under an excitation wavelength of 350 nm. The sharp

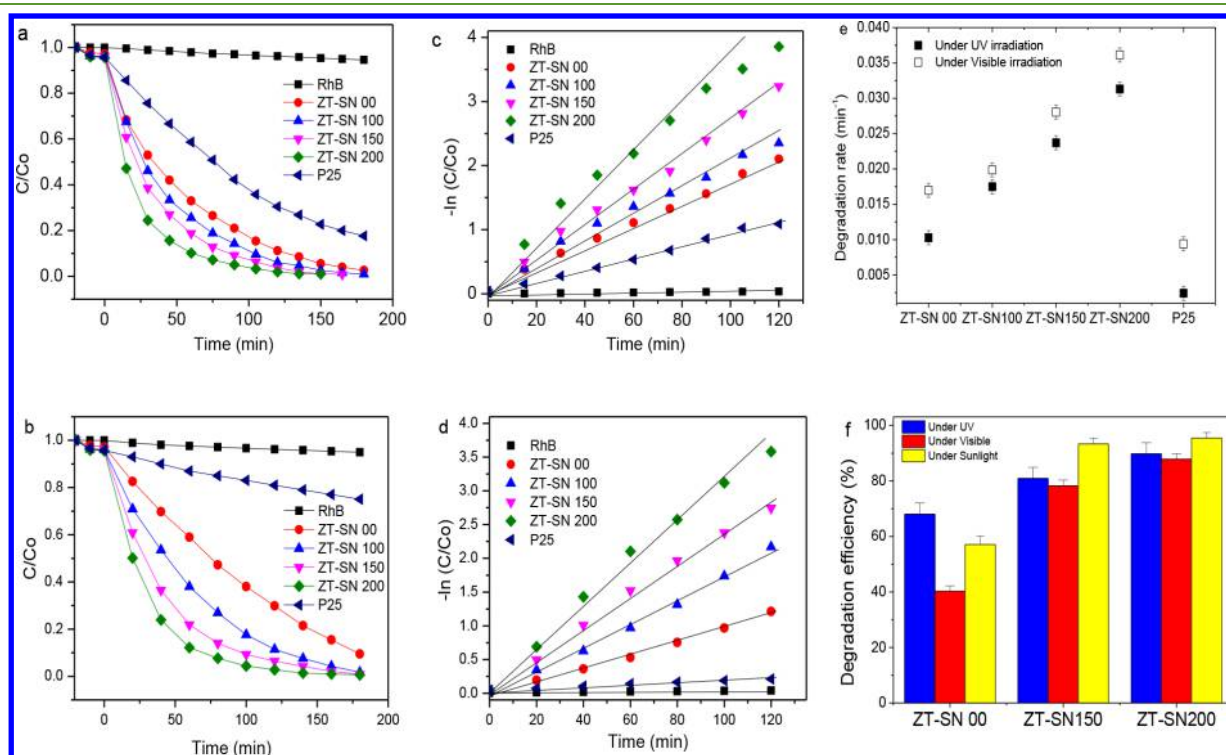


**Figure 6.** Photoluminescence spectra of the pristine and S/N functionalized ZT-SN based NFs.

emission around 397 nm represents the band edge emission of the  $\text{ZnTiO}_3$  layer. The weak and broad emissions around 456 and 548 nm denote the shallow and deep trap states due to the surface defect states.<sup>36</sup> As compared with the pristine NF, on functionalizing, the S/N impurities suppress the deep trap state defect emission, which is caused by the oxygen vacancy states. Shift in the band edge emission reveals a change in band function with respect to the hydrothermal temperature, which is a result of surface functionalization by S and N ions. As the wall of  $\text{ZnTiO}_3$  was converted to  $\text{ZnS}$ , the band edge emission was blue-shifted due to the wide band function of the  $\text{ZnS}$ . The shift in the shallow-trap/self-trap state emission to 445 nm as a

function of the hydrothermal process temperature reveals the structural modification in the band level. This emission may be due to the self-trapped excitons (STE) located at  $\text{TiO}_6$  octahedra that arise owing to the favorable interaction of the Ti 3d orbital with the O 2p orbital due to the structural modification on the  $\text{ZnTiO}_3$  layer. The intense emission signifies the presence of localized surface states within the band gap. As observed from the XPS results, the hydrothermal reaction with L-cysteine induces sulfur and nitrogen based passivated traps which narrow the band function. As a function of hydrothermal temperature, the surface state emission at 445 nm gets intense due to the electron–hole recombination from impurity levels in the  $\text{ZnTiO}_3$  layer. Additionally, the intense emission at 445 nm may be due to the S interstitials based defect states on the  $\text{ZnTiO}_3$  surface. The strong interaction of  $\text{S}^{2-}$  with the function of hydrothermal temperature leads to the intense emission behavior. From this observation, hydrothermal treatment of L-cysteine on the  $\text{ZnTiO}_3$  wall surface initiates the sulfur based defect sites which leads to the narrow band function.

**Photocatalytic Properties.** The effect of S/N cofunctionality effectively induced the enhanced visible absorption in the ZT-SN NFs. To utilize this extended functionality, photocatalytic degradation of an organic dye molecule (RhB) was investigated under the UV ( $\lambda = 365$  nm) and visible irradiation ( $\lambda > 400$  nm), and their time responsive absorption spectra under photoirradiation is presented in Figure S10. The RhB dye molecule has exhibited a self-degradation of 7% under visible degradation in 180 min. In the dark, catalytic NFs exhibit nearly 4–7% of dye adsorption, which is due to absorption of dye molecules on the functionalized surface. An observation of ZT-SN 200 NFs shows a high absorption of dye



**Figure 7.** Photocatalytic properties of surface modified ZT-SN NFs on RhB dye solution. (a,b) Photocatalytic degradation efficiency, (c,d) kinetic fits of ZT-SN NF under UV irradiation and visible irradiation, and (e) comparison study on the photocatalytic degradation rate under UV irradiation and visible-light irradiation. (f) Catalytic efficiency of the ZT-SN NFs for different irradiation sources in 60 min.



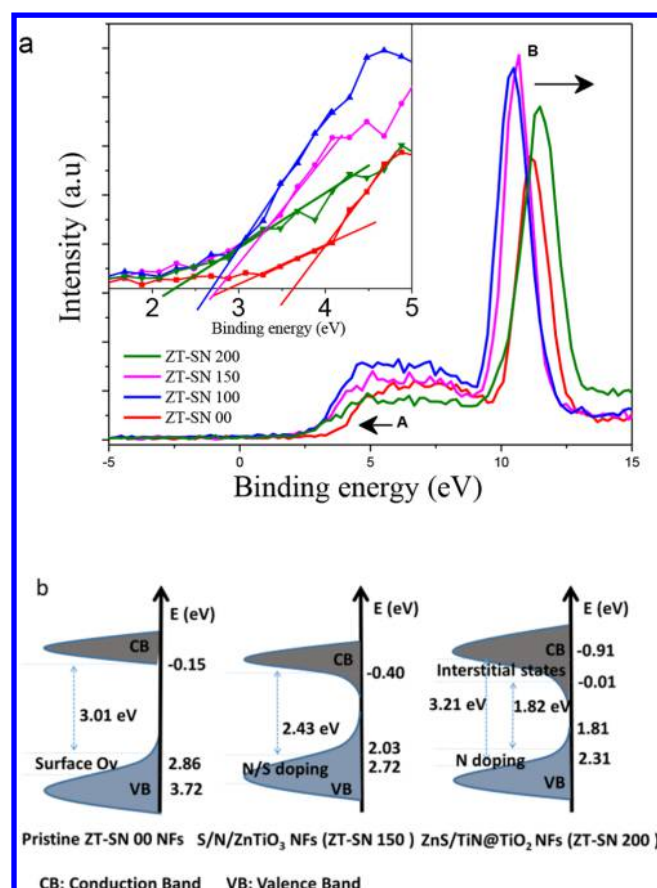
molecules in the dark as compared to the rest of the samples (Figure S11). In Figure 7a, ZT-SN NF exhibits the degradation efficiency of 88.8, 94.1, 96.3, 98.1, and 68.9% for pristine ZT-SN 00 NF, ZT-SN 100, ZT-SN 150, ZT-SN 200, and P25 catalysts, respectively, under UV irradiation of 120 min. Under visible irradiation, the same set of catalysts exhibits RhB decomposition levels of 70.1, 88.7, 93.6, 97.6, and 18.9% for pristine ZT-SN 00 NF, ZT-SN 100, ZT-SN 150, and ZT-SN 200 catalysts, respectively, in 120 min. Table S2 shows the photoresponsive behavior of the ZT-SN NF with respect to the hydrothermal sulfidation temperature. The pristine ZT-SN 00 NFs show a degradation activity around 70.1% in 120 min of visible irradiation, which represents narrow band function (3.01 eV) when compared with bulk  $\text{ZnTiO}_3$  (3.67 eV).<sup>37</sup> When compared with the pristine NF, ZT-SN based samples show faster catalytic behavior under UV and visible irradiation, representing the S and N induced defect levels, thereby favoring effective carrier separation efficiency and promoting visible absorption behavior. The degradation activity fits the pseudo-first-order kinetics, and from the kinetic plot (Figure 7c,d), the degradation rates were calculated and compared with different photoirradiation (Figure 7e). Under visible irradiation, ZT-SN 200 samples exhibited the highest degradation rate of  $0.0314 \text{ min}^{-1}$ , which is about 3.11 times, 1.78 times, and 1.46 times higher than that of pristine ZT-SN 00, ZT-SN 100, and ZT-SN 150 samples, respectively. A similar trend is observed in UV irradiation as well as natural sunlight irradiation, but the photonic intensity under UV irradiation was low as compared to visible irradiation. With the low photonic energy, catalysts were highly active under UV irradiation as with the photonic energy from the visible sources. The Figure 7f shows the photocatalytic efficiency of a ZT-SN based catalyst under different irradiation sources at 60 min of photoirradiation. From the observation, ZT-SN 200 exhibited superior catalytic efficiency under all respective sources and exhibited promising catalytic activity in natural sunlight irradiation. Other organic pollutants such as MB and CP also exhibited the same degradation trend with nearly similar degradation rate differences (Figure S12).

The results show that L-cysteine effectively works as a sulfur and nitrogen source for the effect of band gap narrowing and with visible light activity. The reason behind the extended visible catalytic behavior of the S/N modified ZT-SN NFs was attributed to the S elements introduced on the  $\text{ZnTiO}_3$  lattice, which narrow the band function with the sulfur based defect states below the CB. In general, we can denote the substitution role of N and S interaction with the band structures of the  $\text{ZnTiO}_3$  layer for the favorable visible catalytic activity by the effective separation of carriers through the sub-band levels, but interestingly, we observe that at higher sulfidation temperature,  $\text{ZnTiO}_3/\text{TiO}_2$  transformed into the  $\text{ZnS}/\text{Ti}-\text{N}/\text{TiO}_2$  hierarchical structure. On accounting their individual counter parts, both have a wide band gap nature, but in the form of heterostructural nature, they exhibited a promising visible catalytic activity. Further, the exhibition of  $\text{C}=\text{O}$  in the XPS results of O 1s spectra reveals the presence of C functionality or doping on the fiber surface due to the decomposition of L-cysteine. On comparing with the low temperature growth ZT-SN NF,  $\text{ZnS}/\text{TiN}/\text{TiO}_2$  (ZT-SN 200) NFs shows faster catalytic activity under UV and visible irradiation. The formation mechanism of this structure is not clearly understood, but the  $\text{ZnS}/\text{TiN}/\text{TiO}_2$  form of hierarchical structure exhibited a superior catalytic efficiency. Similar to the catalytic

performance, optical responses evidence the enhancement toward the visible region, which is confirmed from the UV and PL results. In the bulk form, the CB and VB position of  $\text{TiO}_2$  is more positive when compared with the  $\text{ZnS}/\text{TiN}$  leading to the type-I band structure, which inhibits the carrier reaching the catalytic surface. However, the transformation of  $\text{ZnTiO}_3$  into  $\text{ZnS}/\text{TiN}$  based layer enhances the carrier lifetime by changing the band edge positions to result in the effective carrier separation with narrow band function at the heterostructural interface.

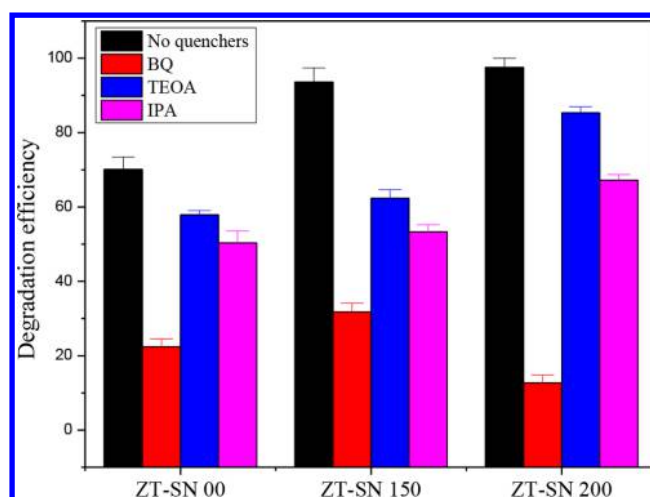
The presence of S and N ion on the  $\text{ZnTiO}_3$  surface induces change in spectral response toward the visible region. Under  $150^\circ\text{C}$  of hydrothermal treatment, the acquired NFs get the S and N doping functionality of the  $\text{ZnTiO}_3$  layer, but at  $200^\circ\text{C}$ , it clearly picturized the heterostructure structure of  $\text{ZnS}/\text{TiO}_2$  with the TiN intergrains. The presence of TiN intergrains was confirmed by the XRD and image mapping results (Figure 3i), but below  $200^\circ\text{C}$  of hydrothermal treatment, the sulfur ions interact in the form of  $\text{SO}_4$  with interstitial ionic states on the NF surface. Sulfur interaction on the catalytic surface with N doping leads to accessible visible absorption with spatial transition of charge carriers. The CB and VB positions were calculated over the surface modified ZT-SN NFs to endorse the band function and to study the possibility of carrier transportation under photoirradiation. The band position with respect to the surface defect states were implicated by calculating the valence and CB position with respect to the surface functionalities of the ZT-SN NF. Figure 8 shows the XPS VB spectra of the S/N form of the surface functionalized  $\text{ZnTiO}_3$  layer. The positions representing A and B in Figure 8 were identified as valence and d-orbital peaks, respectively. The pristine ZT-SN NF has the VB maximum edge at 3.72 eV with the strong tail in valence band function up to 2.86 eV due to the presence of surface oxygen defect states. Further, coupling the calculated band gap from UV DRS spectra (3.01 eV), the position of the CB minimum would occur at  $-0.15 \text{ eV}$ . With the hydrothermal treatment at  $150^\circ\text{C}$  and below, the VB maxima shifted mildly to 2.72 eV band function with a tail at 2.03 eV (Figure S13), which might be due to the N and S doping on the  $\text{ZnTiO}_3$  layer. Under  $200^\circ\text{C}$  of hydrothermal treatment, the VB maxima shifted to 2.31 eV with a mild band function tail at 1.81 eV (Figure S13), which represent the change in VB positions due to C and N doping on the NF surface. The shift toward the lower binding energy values (to the right) implies that the VB position has risen with respect to the sulfidation temperature. Correlating with the calculated band gap from the UV-DRS spectra, the CB minimum suggests  $\sim 0.55$  and  $-0.40 \text{ eV}$  for the ZT-SN 100 and ZT-SN 150 NF, respectively, but because of the two band edges absorbed (in DRS spectra) on the ZT-SN 200 NF, the discrete CB minima lie between  $-0.91 \text{ eV}$  and  $-0.01 \text{ eV}$ . The CB minima at  $-0.91 \text{ eV}$  represent the solid core feature of the  $\text{ZnS}$  or  $\text{TiO}_2$ , and the  $-0.01 \text{ eV}$  represents the extended band function due to the transformation of the  $\text{ZnTiO}_3$  surface to  $\text{ZnS}$  with TiN interfaces. Figure 8b represents the schematic illustration of density of states (DOS) of the surface modified ZT-SN NFs with narrow band function. The N doping functionality leads to a shift in the VB position. Furthermore, the role of S on the  $\text{ZnTiO}_3$  layer induces the narrow band gap by inducing a change in CB position.

The possibility of the band energy shift in the CB and CB position was demonstrated by the XPS and UV visible DRS results. The huge shift in the VB spectra represented the d-



**Figure 8.** (a) Valence-band XPS spectra of the pristine ZT-SN 00 NF and surface modified ZT-SN NF samples. (b) Schematic illustration of the DOS of surface modified ZT-SN NF, as compared to that of the pristine one.

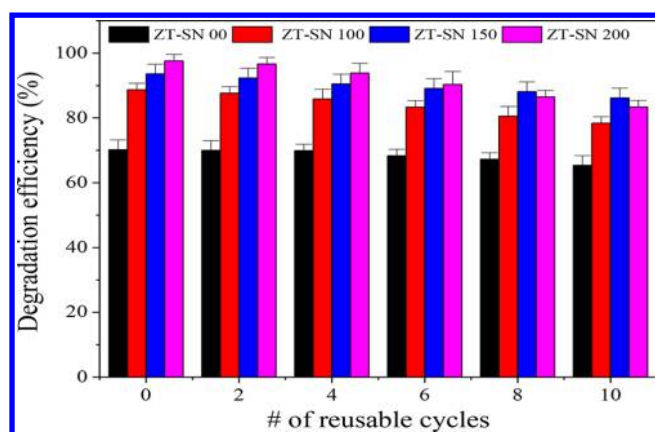
spacing peaks, confirming the transformation of ZnTiO<sub>3</sub> into ZnS/TiN during the hydrothermal process. The dual role of N and S based defects is to induce narrow band functionality with a shift in the *d*-spacing peaks. N-doping may induce an upper lift of the VB position, which minimizes the band function of the ZnTiO<sub>3</sub> layer.<sup>38</sup> The presence of sulfur interstitials and sulfur defect bands creates discrete band levels below the CB position through the localized surface states, which minimize the CB position with narrow band function. The presence of S and N defects is attributed to the tail function in the CB position favoring the band narrowing functionality in the ZnTiO<sub>3</sub> layer. While modifying the ZT-SN NF with L-cysteine at different hydrothermal temperatures, we observed that the interactive nature of the S ions initiate the tailing of the CB through the surface defect states. The presence of S interstitials and the O–Zn–S based surface functionalities on the catalytic surface are promising defect functional levels which minimized the CB position with tailing in the band position. The experimental results motivated us to understand the possible visible catalytic response on the hybrid composite catalyst. The production rate of reactive oxygen species (ROS) was quantified to understand the feasible mechanism of the surface functionality of ZT-SN NF under visible irradiation (Figure S14). Under visible irradiation, the trapping results (Figure 9) with the production of photoinduced holes (h<sup>+</sup>), hydroxyl radicals (°OH) and superoxide radicals (O<sub>2</sub><sup>•−</sup>) were investigated in a way similar to that in the photocatalytic experiment. For pristine ZT-SN NF, the catalytic activity over



**Figure 9.** Trapping experiment of the active species during the catalytic reaction with 120 min of Xe lamp irradiation with ZT-SN based catalysts.

RhB decreases effectively by the addition of BQ. On adding IPA and TEOA with RhB, the activity decayed under photoirradiation but not as noteworthy as with BQ addition. The observation proposed that the production rate of O<sub>2</sub><sup>•−</sup> is promising in ZT-SN 00 NFs which is primarily responsible for the catalytic activity. For ZT-SN 150 samples, the photocatalytic degradation activities for RhB decreases with the addition of IPA and BQ but not in the TEOA. It may be due to the effective separation of electron by S defect, which favors the production of superoxide, which later transforms to the hydroxyl radical. However, the photogenerated hole is not influenced greatly in the catalytic properties. However, for the ZT-SN 200 samples, TEOA does not respond much to the catalytic activity, but BQ gives good response and has mild activity under IPA, influencing a swell. The obtained results suggest that under visible light irradiation, ZnS/TiN@TiO<sub>2</sub> (ZT-SN 200) NF samples exhibited effective production of superoxides through photogenerated electrons which play a major role compared to that of the photogenerated holes. As compared with the pristine ZT-SN 00 NF, the production of ROS was high in ZT-SN 150 NF, but in ZT-SN 200 NF samples, mostly superoxides were found to be active on the surface. This may be due to the contribution of the N-doping functionality with sulfur induced defect levels for effective carrier separation under photoirradiation.

Besides the tunable visible catalytic behavior, the catalytic stability was the notable factor which has disturbed the photocorrosion and self-poisoning effect. The reusable catalytic properties were investigated by consecutive degradation cycles under visible irradiation of RhB dye molecules for nearly 10 cycles (Figure 10). After each cycle, the degraded pollutants were removed and refilled with fresh dye solution for the next run. The catalyst exhibited more stable catalytic degradation efficiency for more than 3 cycles while using ZnS/TiN@TiO<sub>2</sub> NFs as the visible active catalyst. After 10 cycles, visible active ZT-SN 150 and ZT-SN 200 NFs exhibited a degradation efficiency of 86.3% and 83.3% after 120 min, but pristine ZT-SN 00 NFs have stable catalytic efficiency even after 8 cycles under similar visible irradiation. After 10 cycles, the pristine ZT-SN 00 NFs exhibited a degradation efficiency of 68.3% after 120 min. These results solidify the surface stability and catalytic durability of the S/N modified ZT-SN NFs, which



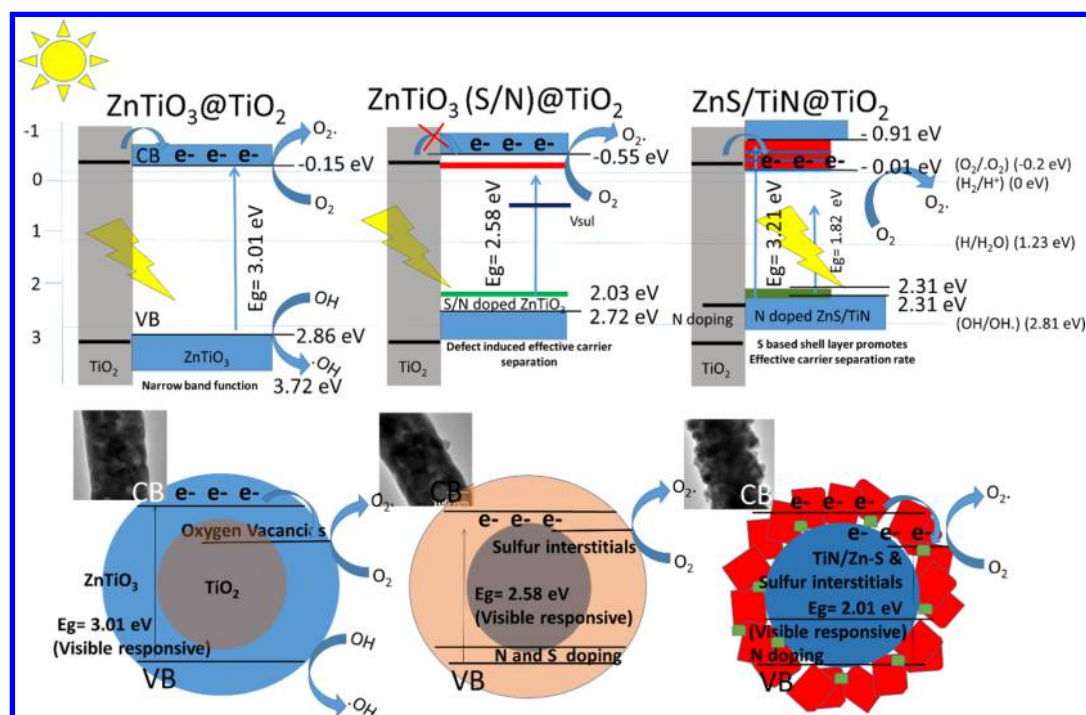
**Figure 10.** Long-term (10 cycles) consecutive photocatalytic degradation of RhB dye solution by using ZT-SN catalysts (15 mg) under indoor sunlight ( $\lambda > 400$  nm) irradiation.

could be a long-term stable catalyst under visible irradiation. The morphological and structural stability of the S/N functionalized ZT-SN NF was nearly stable with 1D assembly after the reusable process under visible irradiation (Figure S15). The XPS results (Figure S16) reveal that after reusable cycles, the atomic ratio of the S/N based functionalities on the catalytic surface started to leach through the photocorrosion process, which further led to minimizing its catalytic efficiency and surface stability. The ICP-MS results revealed 2–3% leaching of Zn ions from ZN-SN 200 indicating poor structural stability of the hierarchical finish, but the ZN-SN 150 and ZN-SN 00 NF catalysts do not exhibit any notable leaching effect during the catalytic cycle. When compared with the hierarchical structural feature, ZT-SN 150 NF catalytic surfaces are more stable because of closely packed grain assemblies,

which lead to effective long-term stability under visible irradiation.

**Proposed Photocatalytic Mechanism.** On the basis of the band function and ROS production rate quantification, the possible mechanism proposed under the visible irradiation of S/N functionalized ZT-SN NF is seen illustrated in the Scheme 2. As ZT-SN 00 NF has a band gap energy of 3.01 eV, it will be active under visible irradiation ( $\lambda > 400$  nm), and further, the presence of  $O_v$  leads to improved photogenerated carrier separation, improving the visible activity. Functionalizing the S/N into the  $ZnTiO_3$  layer at low temperature ( $<200$  °C) leads to  $SO_4$  and S interstitials acting as trap levels below the CB. Further, the functionality of N doped ions may have improvised the VB position for favorable band gap narrowing. The presence of the sulfur induced trap states leads to the delay in carrier recombination rate, and it narrows the band function to improve the visible catalytic efficiency. At higher hydrothermal temperature (200 °C), the catalyst surface was modified to  $ZnS/TiN@TiO_2$  hierarchical structure. The constructed heterostructure leads to visible absorption through sulfur based defect levels in the band function and possible minimization of the VB position by the N- and C-doping nature on the catalyst surface. Furthermore, there are previous investigations on decorating the ZnS surface layer over the wide band gap semiconductors, which shows that it leads to narrow band function at the heterostructural interface due to strained conduction band minimum (CBM) energies.<sup>39</sup> ZnS based surface functionality would influence the work function, and the band bending could be attributed to the electronic hybridization on the catalyst surface<sup>19,40,41</sup> with surface defect states. Further, the N-doping functionality of the ZnS layer leads to reduction in band function for it to be a visibly active one. Additionally, the presence of Ti–N impurities leads to promoted carrier separation and avoidance of the charge

**Scheme 2.** Schematic Representation of the Photocatalytic Mechanism on S/N Functionalized ZT-SN NFs with the Function of Sulfidation Temperature





recombination process. These will lead to improved visible catalytic activity through effective production of photogenerated carriers under visible irradiation.

Observation attained from the optical and XPS results (Figure 4 and Figure 5) reveal that the interaction of S/N functionality leads to narrow band function, which in turn improvised the visible catalytic behavior. Sulfur and nitrogen based defect states on the catalytic surface improvise the carrier separation rate, which also improvised the production rate of ROS on the catalyst surface. As the band potential of the pristine catalyst lies more negative than the reactive potential for the production of superoxide radicals, the photogenerated electrons effectively participate in the catalytic process. Owing to the higher carrier separation efficiency of photogenerated electron and holes on the catalytic surface through the S/N functionality, the heterostructures are a superior photocatalytic system when compared to the pristine one. The production rate of the ROS and effective separation of charge carriers determined the catalytic performance of the NF. On the surface, sulfur and nitrogen based defect level density favors the carrier separation rate by standing in as photogenerated hole trappers,<sup>42</sup> which leads to improvised carrier response for effective catalytic performance under UV and visible irradiation. Trends of the exhibited catalytic performance under UV and visible irradiation were similar. Further, the amounts of photonic density leads to improved catalytic performance as natural solar irradiation is used as the source.

## CONCLUSION

Visible active S/N cofunctionalized Zn-S/TiN decorated TiO<sub>2</sub> as a hierarchical assembly from ZnTiO<sub>3</sub>@TiO<sub>2</sub> NFs was synthesized through electrospinning followed by a hydrothermal process with L-cysteine. Controlling the hydrothermal temperature, the hierarchical surface features of the heterostructural decorations were designed, and their visible responsive properties improved. The existence of N and S in the host lattice leads to narrowing the band function, and these defect levels lead to the improvised production rate of photogenerated charge carriers for effective visible catalytic performance. The hierarchical assembly of ZnS/TiN@TiO<sub>2</sub> NFs displayed faster catalytic activity on RhB dye solution compared to that of the low temperature hydrothermal treated samples. The hydrothermal temperature influences the interaction of S and N with the catalytic surface, enhancing the catalytic rate. The contribution of S induced states with the N-doping functionality on the surface led to the narrow band function and minimized the valence band position, making the NFs visible active. The hierarchical functionality of Ti–N leads to higher carrier separation rate and reduces rapid carrier recombination rate. These features were absent for low temperature annealed hydrothermal treated NFs. Further, reusable properties of NF samples were nearly stable for multiple cycles for the catalytic degradation of RhB dye. To conclude, ZnTiO<sub>3</sub>@TiO<sub>2</sub> and ZnTiO<sub>3</sub>–S/N@TiO<sub>2</sub> NFs could be used as high potential catalysts depending on their surface functionalities to enhance visible photocatalytic efficiency for the degradation of organic pollutants for wastewater treatment.

## ASSOCIATED CONTENT

### Supporting Information

The Supporting Information is available free of charge on the ACS Publications website at DOI: 10.1021/acssuschemeng.8b02455.

SEM images of the as electrospun Zn(OAc)<sub>2</sub>/Ti(OBu)<sub>4</sub>/PVP composite nanofibers and TiO<sub>2</sub>–ZnO composite NFs; HAADF-STEM and STEM EDAX mapping images of ZT-SN 00 NFs; XRD spectrum of ZT-SN 200 NF; EDAX spectra of ZT-SN based NFs; TEM and STEM-EDAX mapping images of ZT-SN 150 NF and ZT-SN 200 NF; BET of ZT-SN 00 and ZT-SN 200 NF; optical images of the ZT-SN based NFs; table related to the XPS results of ZT-SN NFs; optical absorption spectra of RhB under UV and visible irradiation with the presence of catalyst; optical absorption spectra of RhB with catalyst in the dark and without catalyst in visible irradiation; table related to the photoresponsive behavior of ZT-SN based NFs; optical absorption of MB and CP with the presence of ZT-SN based NFs under visible irradiation; valence band spectra of ZT-SN based NFs; reactive oxygen species quantification; SEM images of the reused ZT-SN based NFs; and XPS spectra of the reused ZT-SN based NFs (PDF)

## AUTHOR INFORMATION

### Corresponding Authors

\*(K.S.R.) Tel: +90-3122908987. E-mail: [ranjuphy@gmail.com](mailto:ranjuphy@gmail.com).

\*(T.U.) E-mail: [tamer@unam.bilkent.edu.tr](mailto:tamer@unam.bilkent.edu.tr).

### ORCID

Tamer Uyar: 0000-0002-3989-4481

### Notes

The authors declare no competing financial interest.

## ACKNOWLEDGMENTS

K.S.R. acknowledges The Scientific & Technological Research Council of Turkey (TUBITAK), BIDEB 2216-Fellowships for Research Fellowship Programme for Foreign Citizens for a postdoctoral fellowship.

## REFERENCES

- (1) Khin, M. M.; Nair, A. S.; Babu, V. J.; Murugan, R.; Ramakrishna, S. A review on nanomaterials for environmental remediation. *Energy Environ. Sci.* **2012**, *5*, 8075–8109.
- (2) Safdar, M.; Simmchen, J.; Janis, J. Light-driven micro- and nanomotors for environmental remediation. *Environ. Sci.: Nano* **2017**, *4*, 1602–1616.
- (3) Ansari, S. A.; Khan, M. M.; Kalathil, S.; Nisar, A.; Lee, J.; Cho, M. H. Oxygen vacancy induced band gap narrowing of ZnO nanostructures by an electrochemically active biofilm. *Nanoscale* **2013**, *5* (19), 9238–9246.
- (4) Random, C.; Irvine, J. T. S. Synthesis and visible light photoactivity of a high temperature stable yellow TiO<sub>2</sub> photocatalyst. *J. Mater. Chem.* **2010**, *20* (39), 8700–8704.
- (5) Wu, H.; Min, Y.; Zhang, Q.; Li, W.; Yuan, J.; Wu, Z.; Wang, S. Low-temperature synthesis of mesoporous ZnTiO<sub>3</sub>-graphene composite for the removal of norfloxacin in aqueous solution. *RSC Adv.* **2016**, *6* (105), 103822–103829.
- (6) Pawar, R. C.; Kang, S.; Park, J. H.; Kim, J.; Ahn, S.; Lee, C. S. Evaluation of a multi-dimensional hybrid photocatalyst for enrichment of H<sub>2</sub> evolution and elimination of dye/non-dye pollutants. *Catal. Sci. Technol.* **2017**, *7* (12), 2579–2590.
- (7) Binas, V.; Venieri, D.; Kotzias, D.; Kiriakidis, G. Modified TiO<sub>2</sub> based photocatalysts for improved air and health quality. *J. Materiomics*. **2017**, *3*, 3–16.
- (8) Chen, D.; Wang, Z.; Ren, T.; Ding, H.; Yao, W.; Zong, R.; Zhu, Y. Influence of Defects on the Photocatalytic Activity of ZnO. *J. Phys. Chem. C* **2014**, *118* (28), 15300–15307.

- (9) Yan, H.; Wang, X.; Yao, M.; Yao, X. Band structure design of semiconductors for enhanced photocatalytic activity: The case of  $\text{TiO}_2$ . *Prog. Nat. Sci.* **2013**, *23* (4), 402–407.
- (10) Zaleska, A. Doped- $\text{TiO}_2$ : A Review. *Recent Pat. Eng.* **2008**, *2* (3), 157–164.
- (11) Nada, A. A.; Nasr, M.; Viter, R.; Miele, P.; Roualdes, S.; Bechelany, M. Mesoporous  $\text{ZnFe}_2\text{O}_4/\text{TiO}_2$  Nanofibers Prepared by Electrospinning Coupled to PECVD as Highly Performing Photocatalytic Materials. *J. Phys. Chem. C* **2017**, *121* (44), 24669–24677.
- (12) Nasr, M.; Balme, S.; Eid, C.; Habchi, R.; Miele, P.; Bechelany, M. Enhanced Visible-Light Photocatalytic Performance of Electrospun  $\text{rGO}/\text{TiO}_2$  Composite Nanofibers. *J. Phys. Chem. C* **2017**, *121* (1), 261–269.
- (13) Tan, Y. N.; Wong, C. L.; Mohamed, A. R. An Overview on the Photocatalytic Activity of Nano-Doped- $\text{TiO}_2$  in the Degradation of Organic Pollutants. *ISRN Mater. Sci.* **2011**, *2011*, 1.
- (14) Xing, Z.; Ju, Z.; Zhao, Y.; Wan, J.; Zhu, Y.; Qiang, Y.; Qian, Y. One-pot hydrothermal synthesis of Nitrogen-doped graphene as high-performance anode materials for lithium ion batteries. *Sci. Rep.* **2016**, *6*, 26146.
- (15) Shen, K.; Xue, X.; Wang, X.; Hu, X.; Tian, H.; Zheng, W. One-step synthesis of band-tunable N, S co-doped commercial  $\text{TiO}_2$ /graphene quantum dots composites with enhanced photocatalytic activity. *RSC Adv.* **2017**, *7* (38), 23319–23327.
- (16) Wang, P.; Lin, Z.; Su, X.; Tang, Z. Application of Au based nanomaterials in analytical science. *Nano Today* **2017**, *12*, 64–97.
- (17) Niu, S.; Lv, W.; Zhou, G.; He, Y.; Li, B.; Yang, Q. H.; Kang, F. N and S co-doped porous carbon spheres prepared using L-Cysteine as a dual functional agent for high-performance lithium–sulfur batteries. *Chem. Commun.* **2015**, *51* (100), 17720–17723.
- (18) Miao, X.; Yan, X.; Qu, D.; Li, D.; Tao, F. F.; Sun, Z. Red Emissive Nitrogen Co-doped Carbon Dots and Their Application in Ion Detection and Theraonostics. *ACS Appl. Mater. Interfaces* **2017**, *9* (22), 18549–18556.
- (19) Ranjith, K. S.; Senthamizhan, A.; Balusamy, B.; Uyar, T. Nanograined surface shell wall controlled  $\text{ZnO}/\text{ZnS}$  core-shell nanofibers and their shell wall thickness dependent visible photocatalytic properties. *Catal. Sci. Technol.* **2017**, *7* (5), 1167–1180.
- (20) Ranjith, K. S.; Uyar, T. Rational interjecting of Na and S co-catalyzed  $\text{TiO}_2$  based nanofibers: Presence of surface layered  $\text{TiS}_3$  shell grains and sulphur induced defects for efficient visible-light driven photocatalytic properties. *J. Mater. Chem. A* **2017**, *5* (27), 14206–14219.
- (21) Cao, G.; Li, Y.; Zhang, Q.; Wang, H. Fabrication of Hollow Tetrapod-Like  $\text{TiN}$  Nanostructures and Its Electrochemical Property. *J. Am. Ceram. Soc.* **2012**, *95* (8), 2478–2480.
- (22) Howell, I. R.; Giroire, B.; Garcia, A.; Li, S.; Aymonier, C.; Watkins, J. J. Fabrication of plasmonic  $\text{TiN}$  nanostructures by nitridation of nanoimprinted  $\text{TiO}_2$  nanoparticles. *J. Mater. Chem. C* **2018**, *6* (6), 1399–1406.
- (23) Jiang, J.; Yu, R.; Yi, R.; Qin, W.; Qiu, G.; Liu, X. Biomolecule-assisted synthesis of flower-like  $\text{NiS}$  microcrystals via a hydrothermal process. *J. Alloys Compd.* **2010**, *493* (1), 529–534.
- (24) Chang, K.; Chen, W. L-Cysteine-Assisted Synthesis of Layered  $\text{MoS}_2$ /Graphene Composites with Excellent Electrochemical Performances for Lithium Ion Batteries. *ACS Nano* **2011**, *5* (6), 4720–4728.
- (25) Shen, X.; Jiang, Z.; Gao, C.; Xu, Z.; Xie, Z.; Zheng, L. One-step construction of  $\text{ZnS}/\text{C}$  and  $\text{CdS}/\text{C}$  one-dimensional core–shell nanostructures. *J. Mater. Chem.* **2007**, *17*, 1326–1330.
- (26) Brayek, A.; Chaguetmi, S.; Ghoul, M.; Ben Assaker, I.; Souissi, A.; Mouton, L.; Beaunier, P.; Nowak, S.; Mammeri, F.; Chtourou, R.; Ammar, S. Photoelectrochemical properties of nanocrystalline  $\text{ZnS}$  discrete versus continuous coating of  $\text{ZnO}$  nanorods prepared by electrodeposition. *RSC Adv.* **2016**, *6* (37), 30919–30927.
- (27) Bharti, B.; Kumar, S.; Lee, H. N.; Kumar, R. Formation of oxygen vacancies and  $\text{Ti}^{3+}$  state in  $\text{TiO}_2$  thin film and enhanced optical properties by air plasma treatment. *Sci. Rep.* **2016**, *6*, 32355.
- (28) Ataman, E.; Isvoranu, C.; Knudsen, J.; Schulte, K.; Andersen, J. N.; Schnadt, J. Adsorption of L-Cysteine on rutile  $\text{TiO}_2$  (110). *Surf. Sci.* **2011**, *605* (1–2), 179–186.
- (29) Neal, A. L.; Techkarnjanaruk, S.; Dohnalkova, A.; McCready, D.; Peyton, B. M.; Geesey, G. G. Iron sulfides and sulfur species produced at hematite surfaces in the presence of sulfate-reducing bacteria. *Geochim. Cosmochim. Acta* **2001**, *65* (2), 223–235.
- (30) Veamatahau, A.; Jiang, B.; Seifert, T.; Makuta, S.; Latham, K.; Kanehara, M.; Teranishi, T.; Tachibana, Y. Origin of surface trap states in  $\text{CdS}$  quantum dots: relationship between size dependent photoluminescence and sulfur vacancy trap states. *Phys. Chem. Chem. Phys.* **2015**, *17* (4), 2850–2858.
- (31) Wang, M. Z.; Xie, W. J.; Hu, H.; Yu, Y. Q.; Wu, C. Y.; Wang, L.; Luo, L. B. p-type  $\text{ZnS}:\text{N}$  nanowires: Low-temperature solvothermal doping and optoelectronic properties. *Appl. Phys. Lett.* **2013**, *103* (21), 213111.
- (32) Chen, C.; Bai, H.; Chang, C. Effect of Plasma Processing Gas Composition on the Nitrogen-Doping Status and Visible Light Photocatalysis of  $\text{TiO}_2$ . *J. Phys. Chem. C* **2007**, *111* (42), 15228–15235.
- (33) Livraghi, S.; Chierotti, M. R.; Giamello, E.; Magnacca, G.; Paganini, M. C.; Cappelletti, G.; Bianchi, C. L. Nitrogen-Doped Titanium Dioxide Active in Photocatalytic Reactions with Visible Light: A Multi-Technique Characterization of Differently Prepared Materials. *J. Phys. Chem. C* **2008**, *112* (44), 17244–17252.
- (34) Zhang, Z.; Wang, X.; Long, J.; Gu, Q.; Ding, Z.; Fu, X. Nitrogen-doped titanium dioxide visible light photocatalyst: Spectroscopic identification of photoactive centers. *J. Catal.* **2010**, *276* (2), 201–214.
- (35) Bian, J. M.; Li, X. M.; Gao, X. D.; Yu, W. D.; Chen, L. D. Deposition and electrical properties of N–In codoped p-type  $\text{ZnO}$  films by ultrasonic spray pyrolysis. *Appl. Phys. Lett.* **2004**, *84* (4), 541.
- (36) Choudhury, B.; Dey, M.; Choudhury, A. Shallow and deep trap emission and luminescence quenching of  $\text{TiO}_2$  nanoparticles on Cu doping. *Appl. Nanosci.* **2014**, *4* (4), 499–506.
- (37) Raveendra, R. S.; Prashanth, P. A.; Hari Krishna, R.; Bhagya, N. P.; Nagabhushana, B. M.; Raja Naika, H.; Lingaraju, K.; Nagabhushana, H.; Daruka Prasad, B. Synthesis, structural characterization of nano  $\text{ZnTiO}_3$  ceramic: An effective azo dye adsorbent and antibacterial agent. *Journal of Asian Ceramic Societies.* **2014**, *2* (4), 357–365.
- (38) Wu, H. C.; Lin, Y. S.; Lin, S. W. Mechanisms of Visible Light Photocatalysis in N-Doped Anatase  $\text{TiO}_2$  with Oxygen Vacancies from GGA+U Calculations. *Int. J. Photoenergy* **2013**, *2013*, 1–7.
- (39) Schrier, J.; Demchenko, D. O.; Wang, L. W.; Alivisatos, A. P. Optical properties of  $\text{ZnO}/\text{ZnS}$  and  $\text{ZnO}/\text{ZnTe}$  heterostructures for photovoltaic applications. *Nano Lett.* **2007**, *7* (8), 2377–2382.
- (40) Zhang, Z.; Yates, J. T. Band Bending in Semiconductors: Chemical and Physical Consequences at Surfaces and Interfaces. *Chem. Rev.* **2012**, *112* (10), 5520–5551.
- (41) Lin, Y. J.; Tsai, C. L. Changes in surface band bending, surface work function, and sheet resistance of undoped  $\text{ZnO}$  films due to  $(\text{NH}_4)_2\text{S}_x(\text{NH}_4)_2\text{S}_x$  treatment. *J. Appl. Phys.* **2006**, *100* (11), 113721.
- (42) Khan, H.; Swati, I. K.; Younas, M.; Ullah, A. Chelated Nitrogen-Sulphur-Co doped  $\text{TiO}_2$ : Synthesis, Characterization, Mechanistic, and UV/Visible Photocatalytic Studies. *Int. J. Photoenergy* **2017**, *2017*, 1–17.